Vietnam Journal of Science and Technology ***62*** *(5) (2024) 1031-1043*

doi:10.15625/2525-2518/19248

Nonlinear analysis of three-dimensional hyperelastic problems using radial point interpolation method

Hoai Linh Le Nguyen[1, 2], Vay Siu Lo[1, 2], Thien Tich Truong[1, 2], Nha Thanh Nguyen[1, 2, *]

[1]*Department of Engineering Mechanics, Faculty of Applied Science, University of Technology (HCMUT), 268 Ly Thuong Kiet Street, District 10, Ho Chi Minh City 700000, Viet Nam*

[2]*Vietnam National University Ho Chi Minh City (VNU-HCM), Linh Trung Ward, Thu Duc City, Ho Chi Minh City 700000, Viet Nam*

[*]Email: *nhanguyen@hcmut.edu.vn*

Received: 23 October 2023; Accepted for publication: 20 August 2024

Abstract. Hyperelastic materials are primarily common in real life as well as in industry applications, and studying this kind of material is still an active research area. Naturally, the characteristic of hyperelastic material will be expressed when it undergoes large deformation, so the geometrical nonlinear effect should be considered. To analyze the behavior of hyperelastic material, the Neo-Hookean model is imposed in this study because of its simplicity. The model shows the nonlinear behavior when the deformation becomes large due to the nonlinear displacement-strain relation. This constitutive relation also gives a good correlation with experimental data. This study performs a meshless method, namely the radial point interpolation method (RPIM), to analyze the nonlinear behavior of Neo-Hookean hyperelastic material under a finite deformation state in three-dimensional space. The standard Newton-Raphson technique is applied to obtain the nonlinear solutions. Unlike mesh-based approaches, the meshless method shows its advantages in large deformation problems due to its mesh independence. In this paper, the numerical results of three-dimensional problems that undergo large deformation will be calculated and validated with solutions derived from previous studies. By investigating the obtained results, the superior ability of RPIM in hyperelastic problems can be proved.

Keywords: three-dimensional hyperelasticity, large deformation, RPIM, Meshless.

Classification number: 5.4.3

1. INTRODUCTION

Hyperelastic materials can totally return to their original shape after undergoing large deformation. Unlike other ones, they can easily come to a large deformation state and return without any permanent change in shape, and the weight of those is light. Because of those properties, this kind of material is widely used in practice, such as in car tires, elastomeric pads in bridges, damping systems, or even shock-absorbing matters in many different types of devices. Mathematically, in hyperelastic material, the stress is derived from the derivative of the strain energy function with respect to the strain, and the constitutive relation is the derivative of the stress function. So, the strain energy function needs to be chosen appropriately. There are

many kinds of hyperelastic materials [1] depending on the form of the strain energy density function, including Neo-Hookean, Mooney-Rivlin, Ogden, etc. In practice, hyperelastic materials typically work in large deformation states, so it is appropriate to consider the influence of geometrical nonlinearity in the analysis.

The Finite Element Method (FEM) has been widely used in many fields of mechanics and industry in the last few decades [1, 2]. It is an effective and robust method for mechanical analysis. Indeed, it can be applied to most fields of mechanics, such as structural analysis, fluid flow, heat transfer, etc. Up to now, FEM has already been developed well. One of the characteristics of this method is mesh dependence. It can reduce the effectiveness of FEM in some types of problems, such as crack growth problems, large deformation analysis, breakage simulations, etc. In large deformation analysis, the element shape can be distorted in the regions that are subjected to large deformation so that the accuracy of the variable field cannot be warranted. The root of all issues mentioned above is the use of mesh in constructing the interpolation function. The only way to overcome this drawback is to avoid the mesh dependence of FEM. However, it is challenging because the element needs to be predefined, and the interpolation functions must also be defined initially for a fixed type of element.

Because of the motivation to develop a new method that does not depend on predefined meshes, many kinds of meshless methods have been developed [3 - 5]. In the early 1990s, there were huge attempts in research for weak-form meshless methods. Accordingly, a large number of meshless methods were significantly proposed. Examples of these methods include the Element Free Galerkin method (EFG) [6 – 8], the reproducing kernel particle method (RPKM) [9, 10], the radial point interpolation method (RPIM) [4, 11, 12], etc. Theoretically, a meshless method is a method used to establish system algebraic equations for the whole problem domain without using a predefined mesh [4]. In meshless methods, the domain of a problem is represented by a set of scattered nodes. Different from FEM, the meshless method defines a small bounded region, which is also known as the support domain, of a considered point to construct the interpolation functions from a small set of nodes that are included. The elimination of mesh allows the effective use of the meshless method in many kinds of problems.

This approach uses the radial point interpolation algorithm to construct the RPIM shape function of a considered point, which can be easily imposed on three-dimensional problems. The RPIM shape function is high-order continuous and also possesses the Kronecker property, so the essential boundary conditions can be simply applied.

In most cases, three-dimensional structures are ideally modeled into two-dimensional ones. Much former research has analyzed the behavior of a body in two-dimensional space [12 - 14]. Despite the fact that it can reduce the cost of computation, the generality can be lost. Hence, many actual effects of a body are neglected, which leads to failures when analyzing. In some cases, if accuracy is a critical concern, three-dimensional analysis should be performed.

This research studies the large deformation behavior of a hyperelastic material in three-dimensional space, which contains both the effects of geometrical and material nonlinearity. The Neo-Hookean model, which uses the total Lagrangian formulation, is employed for modeling hyperelastic behavior. The radial point interpolation method with 3D shape functions is proposed, and the standard Newton-Raphson method is applied in this research.

This paper is organized as follows: After this Introduction, Section 2 briefly describes hyper-elastic materials with the constitutive equations. After that, the 3D RPIM interpolation function and the weak form are presented in Section 3. Numerical results are shown in Section 4. Lastly, the main findings and comments on the proposed method are set out in Section 5.

2. CONSTITUTIVE EQUATIONS OF HYPERELASTIC MATERIAL

Consider a hyperelastic solid body subjected to some forces and displacements so that its configuration changes from the undeformed (denoted by $\mathbf{x}$) to the deformed (denoted by $\mathbf{X}$). This deformation is characterized by $\mathbf{F}$, which is known as the deformation gradient tensor.

$$F_{ij} = \frac{x_i}{X_j} = \frac{\partial u_i}{\partial X_j} + \delta_{ij} \tag{1}$$

where u_i represents the component of the displacement field, and δ_{ij} is the Kronecker Delta.

For a hyperelastic body, there is the existence of a strain energy density when the body deforms. Generally, the form of a strain energy density function can be expressed as [1]:

$$W(I_1, I_2, I_3) = \sum_{m+n+k}^{\infty} A_{mnk} \left(I_1 - 3\right)^m \left(I_2 - 3\right)^n \left(I_3 - 1\right)^k \tag{2}$$

where A_{mnk} are the coefficients of polynomials, and I_1, I_2, I_3 are three invariants of the right Right-Cauchy strain tensor $\mathbf{C}$, which is expressed in terms of deformation gradient $\mathbf{F}$ or Lagrangian strain tensor $\mathbf{E}$ as

$$\mathbf{C} = \mathbf{F}^T\mathbf{F} = 2\mathbf{E} - \mathbf{1} \tag{3}$$

where $\mathbf{1}$ is the identity matrix. The Second Piola-Kirchhoff stress is derived from the derivative of the strain energy density function with respect to the Lagrangian strain

$$\mathbf{S} = \frac{\partial \mathrm{W}}{\partial \mathbf{E}} = 2\frac{\partial \mathrm{W}}{\partial \mathbf{C}} \tag{4}$$

Also, the constitutive tensor $\mathbf{D}$ is derived from the second-order derivative of the energy density function

$$\mathbf{D} = \frac{\partial^2 \mathrm{W}}{\partial \mathbf{E}^2} = \frac{\partial \mathbf{S}}{\partial \mathbf{E}} \tag{5}$$

The Cauchy stress can be calculated from tensors $\mathbf{F}$ and $\mathbf{S}$ according to the following relationship:

$$\boldsymbol{\sigma} = \frac{1}{J}\mathbf{F}\mathbf{S}\mathbf{F}^T \tag{6}$$

where J is the determinant of the deformation gradient $\mathbf{F}$ which describes the volume change. Moreover, J relates to the third invariant of the strain tensor $\mathbf{C}$

$$J = \det\left(\mathbf{F}\right); I_3 = J^2 \tag{7}$$

The Neo-Hookean model is adopted in this research, the strain energy density function is expressed in terms of I_1 and J as in [12]:

$$W = \frac{1}{2}\mu\left[I_1 - 3 - 2\ln\left(J\right)\right] + \frac{1}{2}\kappa\left(J - 1\right)^2 \tag{8}$$

where μ is the shear modulus, and κ is the bulk modulus. The Second Piola-Kirchhoff stress tensor is derived from the first-order derivative of strain energy density function as follows:

$$\mathbf{S} = \mu\left(\mathbf{1} - \mathbf{C}^{-1}\right) + \kappa\left[\left(J-1\right)J\right]\mathbf{C}^{-1} \tag{9}$$

Also, the constitutive tensor is derived from the second-order derivative of the strain energy density function with respect to Lagrangian strain

$$\mathbf{D} = \left(\frac{\mu}{J^2} + \kappa\right) J_{,\mathbf{E}} \otimes J_{,\mathbf{E}} + \left[\kappa\left(J-1\right) - \frac{\mu}{J}\right] J_{,\mathbf{EE}} \tag{10}$$

where $J_{,\mathbf{E}} = \partial J / \partial \mathbf{E}$ is the second-order tensor, and $J_{,\mathbf{EE}} = \partial^2 J / \partial \mathbf{E}^2 = \partial J_{,\mathbf{E}} / \partial \mathbf{E}$ is the fourth-order tensor.

3. RPIM FORMULAS FOR HYPERELASTICITY

3.1. Radial basic function approximation

The shape functions of a point in the problem domain are constructed from a set of nodes that are bounded by its support domain. The RPIM interpolation can be written as in [5]:

$$u\left(\mathbf{x}\right) = \left[\mathbf{R}^T\left(\mathbf{x}\right) \quad \mathbf{p}^T\left(\mathbf{x}\right)\right]\begin{Bmatrix}\boldsymbol{\alpha}\\ \boldsymbol{\beta}\end{Bmatrix} \tag{11}$$

where $u\left(\mathbf{x}\right)$ is the interpolation field, $\mathbf{R}^T\left(\mathbf{x}\right)$ is the vector radial basic functions (RBFs), $\mathbf{p}^T\left(\mathbf{x}\right)$ is the vector of *m* polynomial basic functions, $\boldsymbol{\alpha}$ is the vector of coefficients for RBFs, $\boldsymbol{\beta}$ is the vector of coefficients for polynomial.

Eq. (11) satisfies all nodes in the support domain of an interested node at $\mathbf{x}$. From that, a set of linear equations can be formed in matrix form as below:

$$\tilde{\mathbf{U}} = \begin{Bmatrix}\mathbf{U}\\ \mathbf{0}\end{Bmatrix} = \begin{bmatrix}\mathbf{R} & \mathbf{P}\\ \mathbf{P}^T & \mathbf{0}\end{bmatrix}\begin{Bmatrix}\boldsymbol{\alpha}\\ \boldsymbol{\beta}\end{Bmatrix} \equiv \mathbf{Ma} \tag{12}$$

$\mathbf{R}$ is the moment matrix of RBFs

$$\mathbf{R} = \begin{bmatrix} R_1\left(r_1\right) & R_1\left(r_2\right) & \dots & R_1\left(r_n\right)\\ R_2\left(r_1\right) & R_2\left(r_2\right) & \dots & R_2\left(r_n\right)\\ \dots & \dots & \dots & \dots\\ R_n\left(r_1\right) & R_2\left(r_2\right) & \dots & R_n\left(r_n\right)\end{bmatrix}_{n\times n} \tag{13}$$

$\mathbf{P}$ is the moment matrix of polynomial

$$\mathbf{P} = \begin{bmatrix} 1 & x_1 & y_1 & z_1 & \dots\\ 1 & x_2 & y_2 & z_2 & \dots\\ 1 & x_3 & y_3 & z_3 & \dots\\ \dots & \dots & \dots & \dots & \dots\\ 1 & x_n & y_n & z_n & \dots\end{bmatrix}_{n\times m} \tag{14}$$

and $\mathbf{U}$ is the vector containing function values.

Then, Eq. (11) can be rewritten as

$$u(\mathbf{x}) = \left[\mathbf{R}^T(\mathbf{x}) \quad \mathbf{p}^T(\mathbf{x})\right]\mathbf{M}^{-1}\tilde{\mathbf{U}} = \tilde{\mathbf{\Phi}}^T(\mathbf{x})\tilde{\mathbf{U}} \tag{15}$$

where $\tilde{\mathbf{\Phi}}^T$ is the vector of shape functions

$$\begin{aligned}\tilde{\mathbf{\Phi}}^T(\mathbf{x}) &= \left[\mathbf{R}^T(\mathbf{x}) \quad \mathbf{p}^T(\mathbf{x})\right]\mathbf{M}^{-1} \\ &= \left\{\phi_1(\mathbf{x}) \;\; \phi_2(\mathbf{x}) \;\; \cdots \;\; \phi_n(\mathbf{x}) \;\; \ldots \;\; \phi_{n+1}(\mathbf{x}) \;\; \ldots \;\; \phi_{n+m}(\mathbf{x})\right\}^T\end{aligned} \tag{16}$$

Lastly, the vector containing shape functions $\mathbf{\Phi}^T(\mathbf{x})$ can be obtained:

$$\mathbf{\Phi}^T(\mathbf{x}) = \left\{\phi_1(\mathbf{x}) \;\; \phi_2(\mathbf{x}) \;\; \cdots \;\; \phi_n(\mathbf{x})\right\}^T \tag{17}$$

The nodal field can be expressed as

$$u(\mathbf{x}) = \mathbf{\Phi}^T(\mathbf{x})\mathbf{U} = \sum_{i=1}^{n}\phi_i u_i \tag{18}$$

Also, the derivative of $u(\mathbf{x})$ can be obtained effortlessly:

$$u_{,k}(\mathbf{x}) = \mathbf{\Phi}^T{}_{,k}(\mathbf{x})\mathbf{U} = \sum_{i=1}^{n}\phi_{i,k}u_i \tag{19}$$

3.2. The weak form

Given a continuum of a three-dimensional hyperelastic solid body with a volume Ω, bounded by a surface boundary Γ, shown in Figure 1. The body is in equilibrium under the action of external traction force $\mathbf{t}^*$ on surface boundary Γ_t, prescribed displacements on Γ_u and body force $\mathbf{f}^b$.Then, the weak form can be obtained by applying the principle of minimum potential energy and written as in [1]:

$$\int_\Omega \mathbf{S} : \bar{\mathbf{E}}\, d\Omega - \int_\Omega \bar{\mathbf{u}}^T\mathbf{f}^b d\Omega - \int_\Gamma \bar{\mathbf{u}}^T\mathbf{t}^* d\Gamma = 0 \tag{20}$$

The first term denotes the internal energy, which is strain energy of the body and the others are the external energy, which is also the work done by the traction and body force. Vector $\bar{\mathbf{u}}$ is the variation of displacement, $\mathbf{S}$ is the second Piola-Kirchhoff stress, and $\bar{\mathbf{E}}$ is the variation of Lagrangian strain.

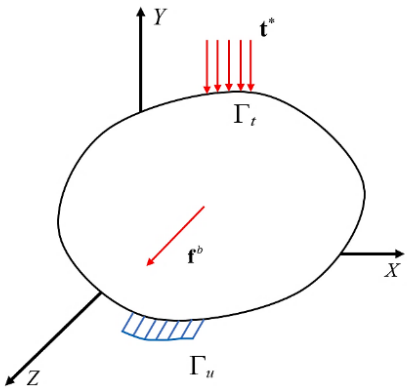

Figure 1. A hyperelastic solid body is in equilibrium.

The discrete version of the weak form is written as

$$\bar{\mathbf{d}}^T \int_\Omega \mathbf{B}_n{}^T \mathbf{S} d\Omega - \sum_{I=1}^{N} \bar{u}_I^T \left\{ \int_\Omega \phi_I \mathbf{f}^b d\Omega + \int_\Gamma \phi_I \mathbf{t}^* d\Gamma \right\} = \bar{\mathbf{d}}^T \left\{ \mathbf{f}^{\text{int}} - \mathbf{f}^{\text{ext}} \right\} = 0 \tag{21}$$

where $\bar{\mathbf{d}}$ is the variation of the nodal displacement vector, and $\mathbf{B}_n$ is the nonlinear displacement-strain matrix. Assuming Eq. (21) is not satisfied, the residual is then defined as

$$\mathbf{R} = \bar{\mathbf{d}}^T \left\{ \mathbf{f}^{\text{int}} - \mathbf{f}^{\text{ext}} \right\} \tag{22}$$

The Newton-Raphson algorithm requires the linearized form of the residual in each iteration, so the linearizing of residual $\mathbf{R}$ must be performed. Then, the linearized residual is

$$L[\mathbf{R}] = \int_\Omega \left[\bar{\mathbf{E}} : \mathbf{D} : \Delta\mathbf{E} + \mathbf{S} : \Delta\bar{\mathbf{E}} \right] d\Omega = \bar{\mathbf{d}}^T \left[\int_\Omega \mathbf{B}_n{}^T \mathbf{D} \mathbf{B}_n + \mathbf{B}_g{}^T \sum \mathbf{B}_g d\Omega \right] \Delta\mathbf{d} \tag{23}$$

where $\mathbf{B}_g$ is the linear displacement-strain matrix, $\mathbf{D}$ is the constitutive tensor. Tensor $\Delta\mathbf{E}$ and $\Delta\bar{\mathbf{E}}$ are the increment of Lagrangian strain and its variation, respectively. Then, the nonlinear equation $\mathbf{R} = 0$ can be solved by the Newton-Raphson method, iteratively. It can be written in the incremental form as

$$\bar{\mathbf{d}}^T \mathbf{K} \Delta\mathbf{d} = \mathbf{R} \tag{24}$$

where

$$\mathbf{K} = \left[\int_\Omega \mathbf{B}_n{}^T \mathbf{D} \mathbf{B}_n + \mathbf{B}_g{}^T \mathbf{M} \mathbf{B}_g \, d\Omega \right] \tag{25}$$

$\mathbf{M}$ is a matrix that contains the second Piola-Kirchhoff stress components.

4. NUMERICAL RESULTS

4.1. Curved beam problem

In order to validate the accuracy of the proposed 3D RPIM method, the curved beam problem is first studied. The geometry of the curved beam is shown in Figure 2a, with dimensions similar to the example in [12] except that it is three-dimensionalized by extending the thickness along the x-axis. Also, Figure 2a shows the boundary conditions of the problem, which is fixed at the bottom face and subjected to a distributed force f at the right-end face (negative x-axis viewing direction).

The nodal distribution of 672 nodes is shown in Figure 2b. The Neo-Hookean material with the behavior of compressibility is used for this problem, the shear modulus is $\mu = 80.194\, N/mm^2$, and the bulk modulus is $\kappa = 120.291\, N/mm^2$. Five values of distributed load f ($0.2,\ 0.3,\ 0.4,\ 0.5\ N/mm^2$) are considered. The displacement convergence criterion is used to estimate the convergence of the nonlinear solution with a predefined tolerance of 10^{-6}.

The accuracy of RPIM is investigated by comparing the displacement in the z-direction of point P with the result in [12], as shown in Table 1. The difference between the two solutions is relatively small, about 1.2 % for all different values of load f.

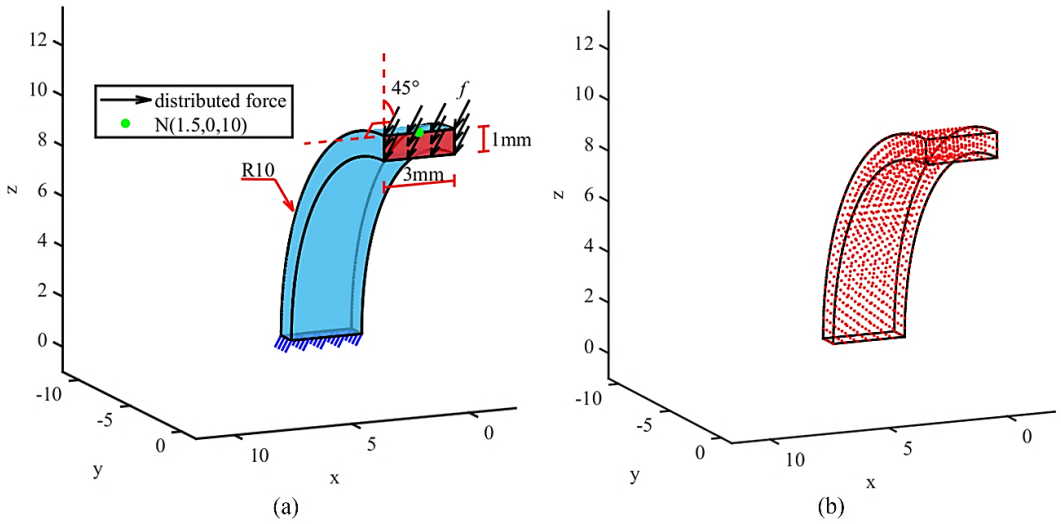

Figure 2. a) Geometry and boundary conditions, b) Distribution of nodes.

To examine the convergence of RPIM, various values of nodal distribution number N (including four values: 672, 1120, 1820, 3234 nodes) are conjugated with various fixed-number of nodes in the support domain n (including six values: 15, 25, 35, 50, 70, 90 nodes). Assuming the displacement along the z-direction of point P is a function of n and N, then $u_z = u_z(n, N)$. That function is a surface in three-dimensional created from discrete function values at all combinations of n and N, shown in Figure 3. Also, the green line contains all converged values at every fixed value of N. In contrast, the blue line includes all converged values at every fixed value of n. Hence, the intersection of those lines (the magenta point) is the desired converged combination of n and N (n = 35, N = 1120).

Then, the converged result of point P at various values of load f is shown in Figure 4. The deformed geometries of the beam at five values of load f are plotted in Figure 5. Because the stress components S_{xx}, S_{xy}, and S_{xz} are small compared to other components (S_{yy}, S_{zz}, S_{yz}), only S_{yy}, S_{zz}, and S_{yz} components of the second Piola-Kirchhoff stress are shown in Figure 6.

Table 1. The comparison of z-displacement, u_z, at point P.

f (N/mm^2)	z-displacement of point P (mm)		
	RPIM (672 nodes)	iRPIM	Error (%)
0.2	–6.2757	–6.3523	1.20586
0.3	–11.1948	–11.3343	1.23078
0.4	–13.7247	–13.8685	1.03688
0.5	–15.0610	–15.1995	0.91121

Consider nodes whose coordinate is $\{x_i, -8.59, 5.12\}^T : x_i \in (0,\ 0.5,\ 1,\ 1.5,\ 2,\ 2.5,\ 3)$ as shown in Figure 7a. The displacement components of those are not exactly the same along the x-direction. As shown in Figure 7b, the x-displacement of a node is slightly higher as it gets closer to the boundary. In contrast, the y- and z-displacements tend to decrease, as shown in Figure 7c, and Figure 7d. This shows precisely the natural behavior of a beam subjected to a shearing force.

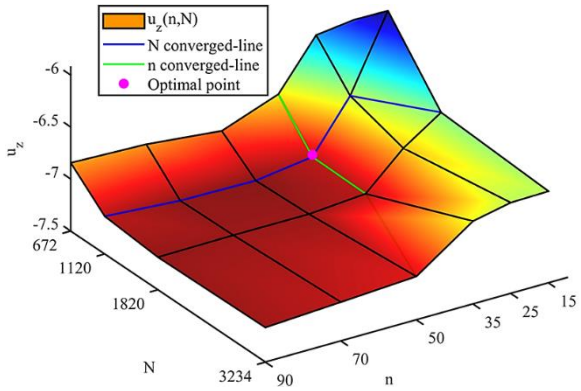

Figure 3. Convergence surface of RPIM.

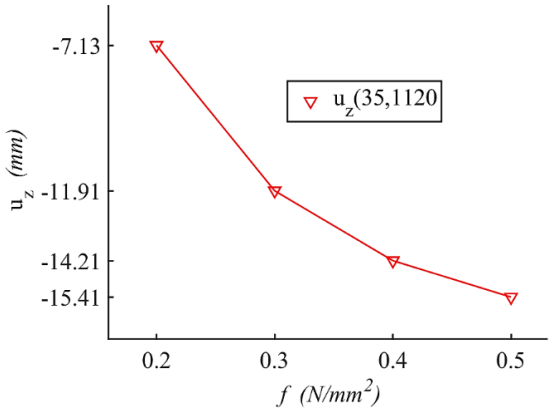

Figure 4. Converged result of point P at various values of load *f*.

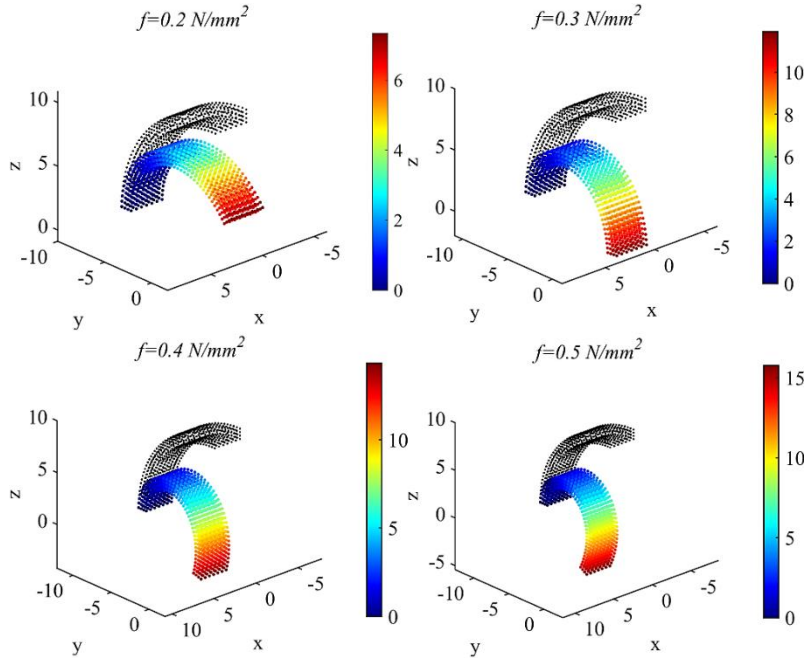

Figure 5. Deformed geometries of the beam subjected to various values of distributed load *f*.

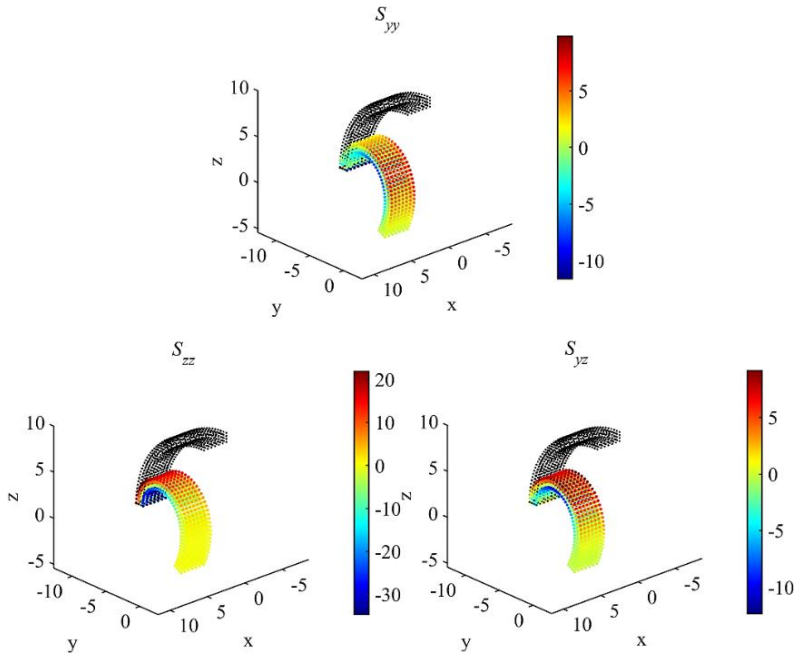

Figure 6. Components of the second Piola-Kirchhoff stress of the beam under load $f = 0.5N/mm^2$.

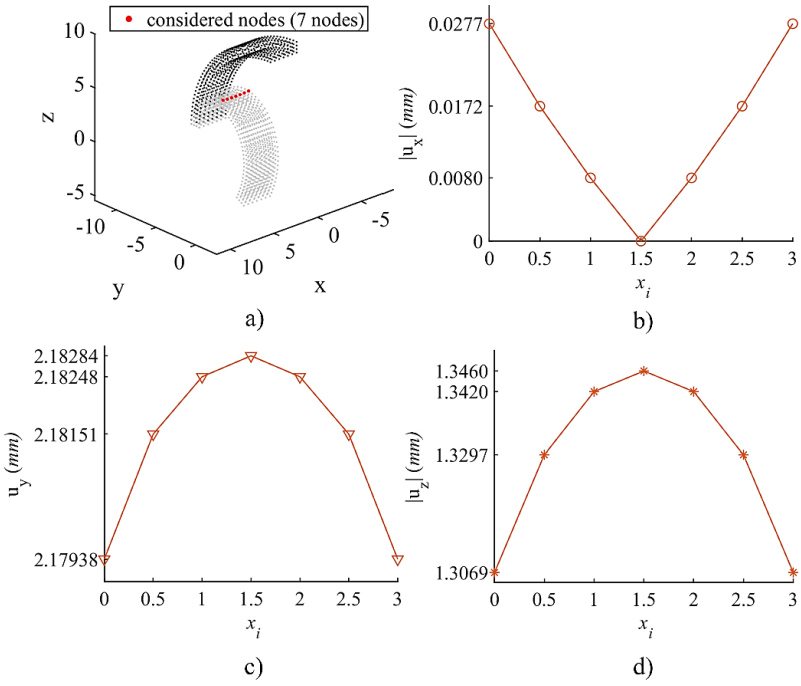

Figure 7. Distribution of displacement components along the x-axis under load $f = 0.5N/mm^2$.

4.2. Cook's membrane problem

The second problem is Cook's membrane [12]. Its dimensions are shown in Figure 8, it is fixed at the left end face and subjected to a distributed force f on the right end face. The Neo-

Hookean material is used to mathematically describe the compressible behavior of the problem. Also, its shear modulus and bulk modulus are $\mu = 80.194\,N/mm^2$ and $\kappa = 120.291\,N/mm^2$, respectively. Firstly, the convergence of RPIM needs to be studied under the action of the force $f = 8\,N/mm^2$. It is the same as the previous problem, various combinations of two parameters, *n* and *N*, are conjugated to calculate the z-displacement of considered point *P* (shown in Figure 8) for investigating the most converged one. Then, the most converged combination of *n* and *N* is (65, 2268), the nodal distribution of *N* = 2268 nodes is plotted in Figure 9. The accuracy of RPIM is evaluated by comparing its results with the reference results obtained from the Finite Element method (ANSYS), as shown in Table 2. Note that the error in the table is calculated by comparing with ground-true results obtained from the Finite Element method with a very fine mesh. Accordingly, the rate of convergence of PRIM can be visualized in the comparison table.

Table 2. Displacement in z-direction at point *P*, u_z, obtained using RPIM and FEM.

$f(\frac{N}{mm^2})$	RPIM (2268 nodes)				FEM (2268 nodes)	
	$u_z\,(n=45)$	Error (%)	$u_z\,(n=65)$	Error (%)	u_z	Error (%)
8	11.434	0.0147	11.433	0.0094	11.347	0.7435
12	14.818	0.1216	14.813	0.0911	14.731	0.4662
16	17.470	0.1874	17.453	0.0912	17.376	0.3498
20	19.701	0.2197	19.669	0.0558	19.593	0.3307

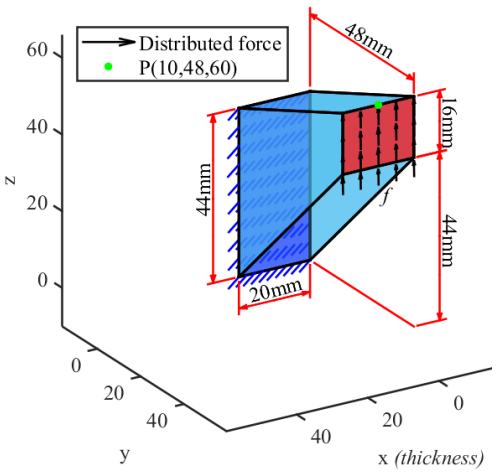

Figure 8. Geometry of the membrane.

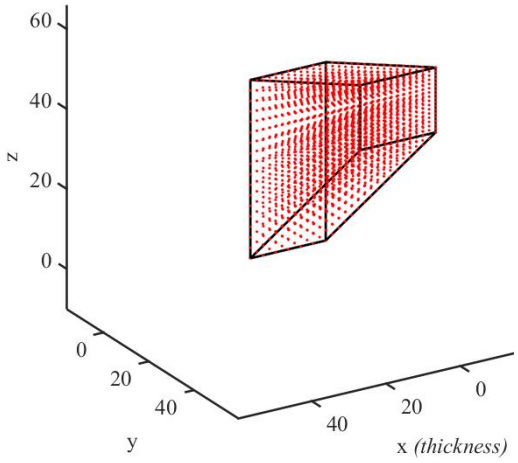

Figure 9. Nodal distribution of 2268 nodes.

Using the nodal distribution of *N* = 2268 and the fixed number of nodes in the support domain *n* = 65, various values of load *f* are subjected to the body in order to find its behavior under the condition of large deformation. The deformed configurations of the membrane under various values of load *f* are shown in Figure 10. Moreover, the components of the second Piola-Kirchhoff stress are shown in Figure 11, in the case of load $f = 8\,N/mm^2$.

To investigate the behavior of the displacement along the thickness (x-direction), several nodes whose coordinate is $(x_i,\ 48,\ 60)^T$, $x_i \in (0,\ 3.33,\ 6.66,\ 10,\ 13.33,\ 16.66,\ 20)$ are considered. Figure 12 represents the distributions of displacement components of these nodes

under load $f = 8\,N/mm^2$. Obviously, the displacement components of these nodes are symmetric due to the boundary condition, which cannot be seen if the plane strain analysis is performed.

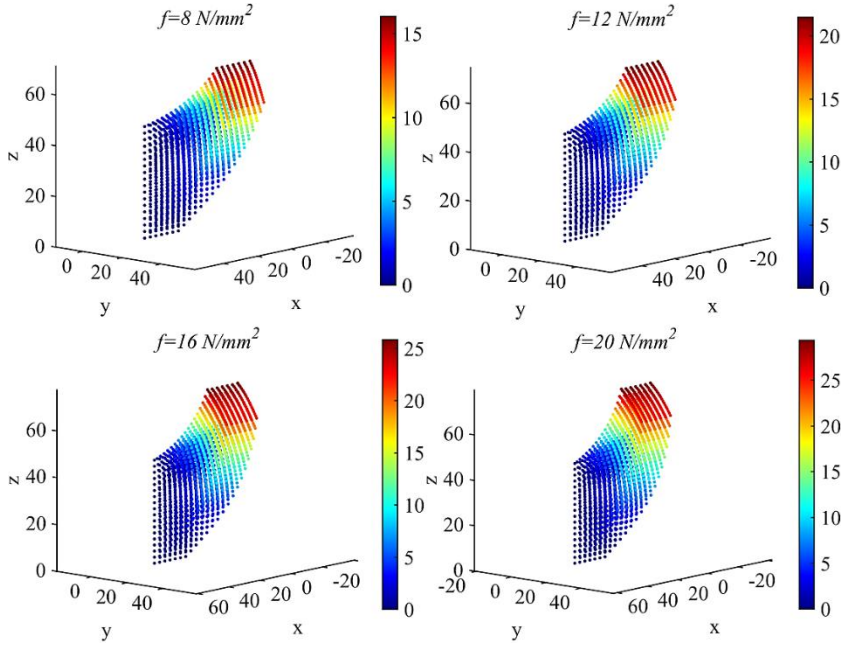

Figure 10. Deformed configurations of the membrane under various values of load *f*.

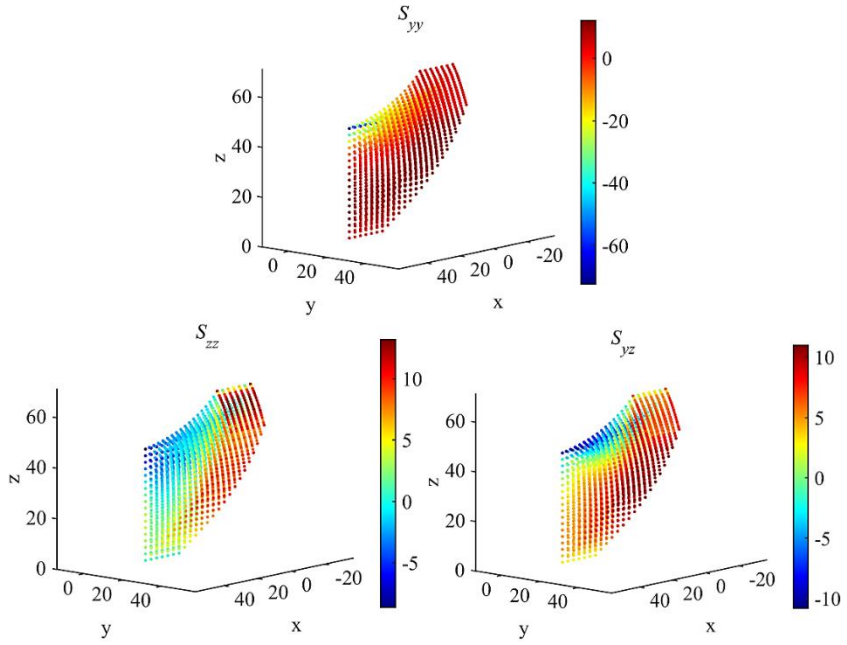

Figure 11. Second Piola-Kirchhoff stress components (N/mm^2) in the case of $f = 8\,N/mm^2$.

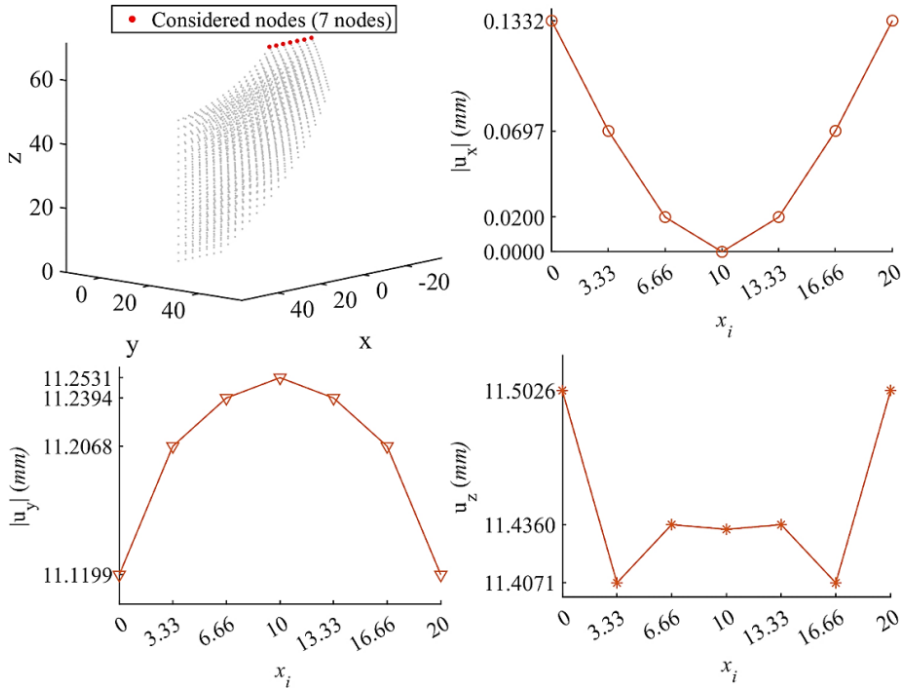

Figure 12. Distributions of displacement components of the considered nodes under load $f = 8N/mm^2$.

5. CONCLUSIONS

In this paper, the behavior of hyperelastic material in a three-dimensional problem is studied using the approach of RPIM. There are two types of non-linearity taken into account in this study including geometric and material behavior. Two hyperelastic material problems are presented to investigate the effective use of meshless methods in the general 3D model, and they both offer good convergence. By using the radial point interpolation algorithm to construct the 3D shape function, the proposed RPIM approach for non-linear problems can give a more accurate solution using the same number of degrees of freedom as conventional finite element analysis. Moreover, RPIM can handle finite-deformation problems well by eliminating the highly distorted behavior of elements, which exists in mesh-based methods. It is also shown that if the actual behavior of a body is a concern, it must be performed as a three-dimensional problem rather than a modelized two-dimensional one. The proposed method can be further applied to more complicated non-linear problems such as crack growth, damage, or contact analysis in hyperelastic material.

Acknowledgements. This research is funded by the Vietnam National University Ho Chi Minh City (VNU-HCM) under grant number B2022-20-02. We acknowledge Ho Chi Minh City University of Technology (HCMUT), VNU-HCM for supporting this study.

CRediT authorship contribution statement. Hoai Linh Le Nguyen: Developer of the method. Vay Siu Lo: Manuscript editor. Thien Tich Truong: Supervision. Nha Thanh Nguyen: Formal analysis.

Declaration of competing interest. The authors declare that they have no known competing financial interests or personal relationships that could have appeared to influence the work reported in this paper.

REFERENCES

1. Nam-Ho K. - Introduction to Nonlinear Finite Element Analysis, Springer, New York, 2015. doi.org/10.1007/978-1-4419-1746-1.
2. Peter W. - Nonlinear Finite Element Methods, Springer, German, 2008. doi.org/10.1007/978-3-540-71001-1.
3. Youping C., James L., Azim E. - Meshless Methods in Solid Mechanics, Springer, United States, 2006. doi.org/10.1007/0-387-33368-1.
4. Gui-Rong L., Yuan-Tong G. - A point interpolation method for two-dimensional solids, Int. J. Numer. Methods. Eng. **50** (4) (2001) 937-951. doi.org/10.1002/1097-0207(20010210)50:4<937::AID-NME62>3.0.CO;2-X.
5. Gui-Rong L. - Mesh free methods: Moving beyond the finite element method, CRC Press, Florida, 2009. doi.org/10.1201/9781420082104.
6. Ted B., Yun-Yun L., and Lei G. - Element Free Galerkin Methods, Int. J. Numer. Methods Eng., **37** (2) (1994) 229–256. doi.org/10.1002/nme.1620370205.
7. XiaoJie C., MiaoJuan P., YuMin C. - The improved element-free Galerkin method for elastoplasticity large deformation problems, Zhongguo Kexue. Wulixue Lixue Tianwenxue, **48** (2) (2018) 024701. doi.org/10.1360/SSPMA2017-00231.
8. Yu S. Y., Miaojuan P., Heng C., Yumin. C. - The improved element-free Galerkin method for three-dimensional elastoplasticity problems, Eng. Anal. Bound. Elem. **104** (2019) 215-224. doi.org/10.1016/j.enganabound.2019.03.040.
9. Wing K. L., Chen Y., Jun S., Jiun-Shyan C., Ted B., Pan C., Uras R. A., & Chang C. T. - Overview and applications of the reproducing Kernel Particle methods, Arch. Comput. Methods Eng. **3** (1) (1996) 3-80. doi.org/10.1007/bf02736130.
10. Zheng L., Gaofeng W., Zhiming W., Jinwei Q. - The Meshfree Analysis of Geometrically Nonlinear Problem Based on Radial Basis Reproducing Kernel Particle Method, Int. J. Appl. Mech. **12** (4) (2020) 2050044. doi.org/10.1142/S1758825120500441.
11. Gui-Rong L, Zhang G. Y., YuanTong G., Wang Y. Y. - A meshfree radial point interpolation method (RPIM) for three-dimensional solids, Computational Mechanics, **36** (6) (2005) 421-430. doi.org/10.1007/s00466-005-0657-6.
12. Nha T. N., Minh N. N., Thien T. T., Tinh Q. B. - An Improved Meshless Method for Finite Deformation Problem in Compressible Hyperelastic Media, Vietnam J. Mech., **43** (1) (2021) 27-41. doi.org/10.15625/0866-7136/15332.
13. Ramtin H., Raza A., Hessam R. - Large deformation analysis of 2D hyperelastic bodies based on the compressible nonlinear elasticity: A numerical variational method, Int. J. Non. Linear Mech. **116** (2019) 39-54. doi.org/10.1016/j.ijnonlinmec.2019.05.003.
14. Thai V. V., Nha T. N., Minh N. N., Thien T. T., Tinh Q. B. - A Meshfree Method Based on Integrated Radial Basis Functions for 2D Hyperelastic Bodies, in: Tien Khiem, N., Van Lien, T., Xuan Hung, N. (eds) Modern Mechanics and Applications, Lecture Notes in Mechanical Engineering, Springer, Singapore, 2022. doi.org/10.1007/978-981-16-3239-6_78.